Trans Indian Inst Met (2025) 78:19
https://doi.org/10.1007/s12666-024-03525-3

ORIGINAL ARTICLE

Selective Synthesis of Mesoporous Magnetic Iron Oxide Nanoparticles via Green Approach: Highly Efficient Adsorption of Malachite Green

Maliheh Yaghoobi[1] · **Fatemeh Asjadi**[2]

Received: 25 January 2024 / Accepted: 6 September 2024 / Published online: 2 January 2025

Abstract Iron oxides were synthesized via green and chemical approach due to importance of this metal oxide in wastewater treatment. The characterization of products was performed utilizing X-ray diffraction (XRD), Fourier transform infrared (FTIR) spectroscopy, Brunauer–Emmett–Teller (BET), and field emission scanning electron microscopy (FE-SEM) analyses. The intervention of plant extract significantly influenced the phase, morphology, size, and porosity of the resulting products. Mesoporous paramagnetic Fe_3O_4 nanoparticles were produced using green method. Conversely, nonporous cubic Fe_2O_3 was formed in the chemical method. The average particle size of spherical Fe_3O_4 nanoparticles was 36.12 nm. The specific surface area and average pore size of the nanoparticles were determined as 165 $m^2.g^{-1}$ and 3.32 nm, respectively. The dye adsorption followed the pseudo-second-order kinetic model, with a maximum capacity of 35.44 $mg.g^{-1}$. Furthermore, the as-prepared Fe_3O_4 nanoparticles exhibited a robust saturation magnetization of 31.09 $emu.g^{-1}$, enhancing their potential for effective application in wastewater treatment.

✉ Maliheh Yaghoobi
myaghoobi@znu.ac.ir

Fatemeh Asjadi
asjodi@znu.ac.ir

[1] Department of Chemical Engineering, Faculty of Engineering, University of Zanjan, P.O. Box 45371-38791, Zanjan, Iran

[2] Department of Materials Science and Engineering, Faculty of Engineering, University of Zanjan, P.O. Box 45371-38791, Zanjan, Iran

Graphical Abstract

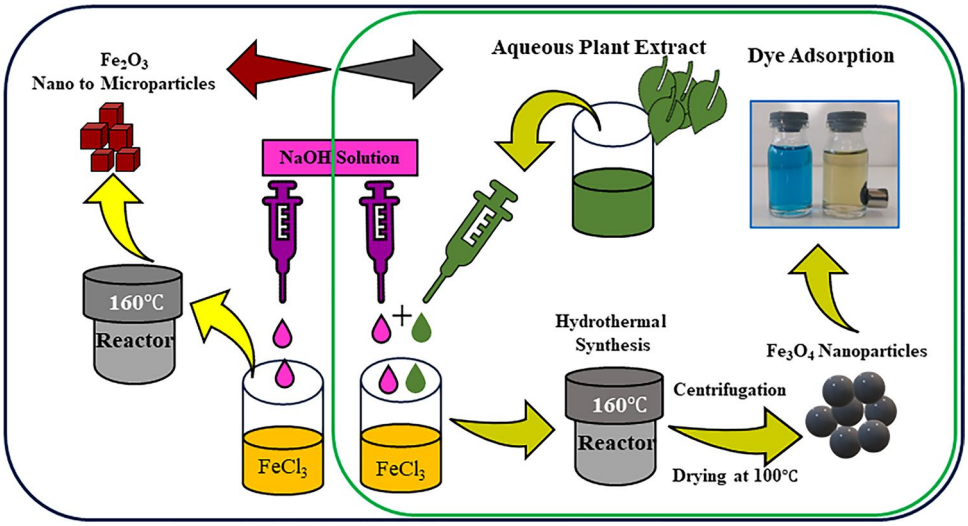

Keywords Paramagnetic Fe_3O_4 · Green hydrothermal synthesis · Mesoporous · Malachite green · Fe_2O_3

1 1 Introduction

Surface water pollution is a growing environmental concern, primarily driven by industrial activities [1]. Finding simple, fast, and low-cost methods for water purification becomes imperative in mitigating these adverse impacts. Among the diverse pollutants, organic dyes emerge as particularly noteworthy contributors to water pollution due to their wide applications in paper, textiles, cosmetics, and many other industries [2]. Malachite green (MG) is an organic compound and highly soluble in water with an N-methylated diaminotriphenylmethane structure [3, 4] commonly applied in various productions, for instance cotton, leather, wool, silk, paper, and printing inks [5]. In addition, the MG is unlawfully used in aquaculture as an antibiotic with antifungal activity [6]. As a Class II Health hazard, the MG generates severe public health hazards and poses potential environmental problems [7].

Despite the numerous water treatment methods available, such as membrane separation process, coagulation, chemical oxidation, and microbial decomposition, many of them are not practically applicable due to drawbacks such as high costs, prolonged processing times, and the need for sophisticated equipment [8]. The adsorption method is a prevalent approach for dye removal from wastewater due to its simplicity and lower cost [9]. Despite the advantages of the adsorption process, the incorporation of filtration post-adsorption poses a challenging task. For instance, activated carbon has long been consumed for organic dye adsorption due to its high specific surface area, porosity, and low cost. Although it has high efficiency in separating organic dyes, its application on a large scale is challenging due to its inherent secondary pollution and the difficulty of separating it from purified water [10, 11]. After the adsorption process, it should be possible to remove the adsorbent from the water so that the adsorbent itself does not cause secondary pollution in the water. For this reason, unlike activated carbon, magnetic nanoparticles are easily separated from water and reused after recovery. Rapid magnetic separation of magnetic adsorbents can serve as a time-efficient alternative to the time-consuming and expensive filtration stage.

The magnetic nanoparticles are the focus of attention due to their large specific surface area and ease of collection from treated wastewater in dye adsorption techniques [12, 13]. Iron oxides are one of the most widely used transition metal oxides in water treatment applications. Most iron oxides are mainly magnetite (Fe_3O_4), maghemite (γ-Fe_2O_3), and hematite (α-Fe_2O_3) [14]. Due to the presence of iron cations in two states (Fe^{+3} and Fe^{+2}) and high magnetic property, the Fe_3O_4 magnetite exhibited unique properties and hold greater potential compared to other iron oxides [15]. Despite these advantages, it is associated with problems such as aggregation and instability in acidic conditions [16]. The surface of theses adsorbents should be modified and stabilized [17, 18]. The green synthesis in the presence of the plant extract enhances the colloidal and chemical stability of the Fe_3O_4 nanoparticles, having high porosity and magnetic properties [19]. Therefore, it emerges as a promising candidate for effective dye adsorption.

In our previous work, our research team utilized iron sulfate as the salt precursor. Synthesis was conducted in both the presence and absence of peppermint extract to produce iron oxide. The results revealed the formation of spherical Fe_3O_4 nanoparticles in both scenarios [20]. In this work, iron chloride was employed as the salt precursor. Syntheses were performed both in the presence of the extract and through chemical means, highlighting the profound influence of the primary salt on the final product and also on the role of plant extract. The X-ray diffraction (XRD), field emission scanning electron microscopy (FE-SEM), Fourier transform infrared (FTIR) spectroscopy, and Brunauer–Emmett–Teller (BET) analyses were applied to characterize the products. The MG dye adsorption was estimated using synthesized magnetic iron oxide nanoparticles, and three kinetic adsorption models were studied.

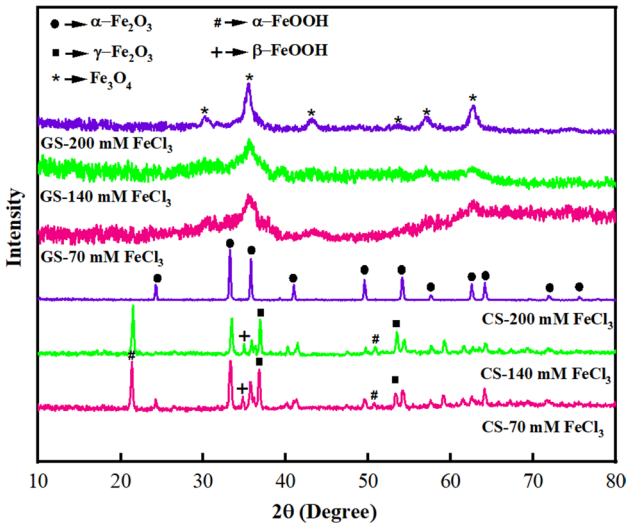

Fig. 1 XRD patterns of green synthesis (GS) and chemical synthesis (CS) of iron oxides

2 Materials and Methods

2.1 Materials

The ferric chloride hexahydrate $FeCl_3.6H_2O$ (99%), malachite green (MG-$C_{52}H_{54}N_4O_{12}$; Mwt 927 g.mol^{-1}; pka = 6.9), and NaOH were purchased from Merck company, Germany. The deionized water was used in all experiments. The myrtle leaves were prepared from greenhouse of University of Zanjan (Zanjan, Iran).

2.2 Synthesis of Iron Oxides

According our recent publication [20], the crushed dry leaves soaked in water in ratio of 1 to 10 g.ml^{-1}. Then, the mixture was heated on stirrer up to 70 °C for two hours and then filtered to obtain extract. All experiments were done in the final solution at three concentrations of precursor: 70, 140, and 200 mM. In the chemical approach, $FeCl_3.6H_2O$ as a precursor salt was dissolved in hot deionized water (70 °C), and the pH was adjusted at 12 using a NaOH solution. The 70 ml of the final reaction solution was poured into a Teflon-lined stainless steel reactor, sealed, and incubated at 160 °C for 15 h. In the green technique, the fresh extract was gradually mixed with iron (III) chloride solution in the same ratio before adjusting pH by 12. The products were collected and dried after washing.

2.3 Characterization of Synthesized Nanoparticles

The produced iron oxide products were carefully characterized via X-ray diffraction (XRD), Fourier transform infrared (FTIR), field emission scanning electron microscopy (FE-SEM), energy-dispersive spectroscopy (EDS), vibrating-sample magnetometry (VSM), and Brunauer–Emmett–Teller (BET) surface area and porosity analyses.

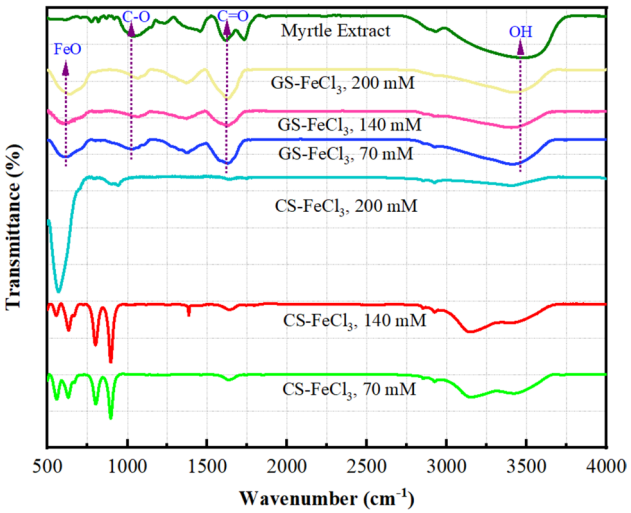

Fig. 2 FTIR spectrum of aqueous myrtle extract, green synthesis (GS) and chemical synthesis (CS) of iron oxides

2.4 Adsorption Experiments

To obtain the adsorption capacity, 0.25g of synthesized Fe_3O_4 powder was added to 50 ml of dye solution at various concentrations of 50, 100, 150, and 200 ppm and shaken. The samples were taken over the adsorption process to determine the color change. The supernatant was filtered to attain a clear solution without any particles. The absorbance of the

supernatant was measured using a visible spectrophotometer at 617 nm.

The amount of adsorbed MG dye was obtained using the following equation [21]:

$$q_t = \left(C_{\mathrm{id}} - C_{\mathrm{td}}\right)\frac{V}{W} \tag{1}$$

where q_t is the quantity of adsorbed dye per one gram of adsorbent at every moment, and C_{id} and C_{td} are the dye concentration in the beginning of adsorption experiments and at every moment, respectively. The volume of the dye solution and the adsorbent mass is presented by V and W, respectively. Also, the dye removal percentage was calculated as follows [22]:

$$\text{Removal}\ (\%) = \frac{\left(C_{\mathrm{id}} - C_{\mathrm{td}}\right)}{C_{\mathrm{id}}} \times 100 \tag{2}$$

3 Results and Discussion

3.1 Effect of Myrtle Extract and Iron Salt Concentration on Phase Formation and Structure of Produced Iron Oxides

The XRD patterns in Fig. 1 show two different types of iron oxide in the presence and absence of the myrtle extract.

In the green synthesized (GS) samples, the XRD pattern exhibited characteristic peaks of Fe_3O_4 nanoparticles at six main positions (2 θ) of 30.1°, 35.5°, 43.2°, 53.5°, 57°, and 62.8° corresponding to planes (220), (311), (400), (422), (511), and (440), respectively [23, 24]. In addition, the broad diffraction peaks were observed in a low concentration of salt. Increasing the iron salt led to decrease the width of peaks. The sharp peaks were created at a high concentration of precursor, which reflects the higher crystallinity of produced Fe_3O_4 nanoparticles compared to other GS samples. On the other hand, different iron oxides were created for the chemically synthesized (CS) samples. The pure α-Fe_2O_3 appeared at a high iron chloride concentration in the CS samples. Eleven diffraction peaks in positions (2θ) of 24.2°, 33.1°, 35.7°, 40.9°, 49.5°, 54.1°, 57.6°, 62.5°, 64.1°, 71.9°, and 75.5° were observed (see CS samples of Fig. 2), which can be related to (012), (104), (110), (113), (024), (116), (122), (214), (300), (1010), and (220) crystal planes of $\alpha-Fe_2O_3$ [25–27]. The pure iron oxide compound was not observed in 70 and 140 mM. The different forms of Fe_2O_3 (α, andγforms) and FeOOH (α, andβforms) were produced in less than a 200 mM. These results reveal the importance of precursor concentration in the hydrothermal route, which other researchers rarely investigated. These results disclose the plant role in reducing iron ions and changing the reaction path.

In addition, the peaks of CS samples are narrower and sharper than GS samples. It implies that the crystallite size of particles produced in the reaction of CS is bigger than GS samples. The crystallite size of samples was estimated using the Debye–Scherrer equation [28]:

$$D = \frac{k\lambda}{\beta\cos\theta} \tag{3}$$

where D is the mean crystallite size, k is a shape factor (usually set to 0.9 for spherical crystallites), λ denotes the wavelength (0.154 nm), β is the full width at half maximum of the peak, and θ represents the Bragg angle. The average crystallite size of GS and CS samples was obtained as 9.09 ± 0.41 and 41.51 ± 4.67 nm, respectively. The average crystallite size, determined by the XRD pattern, is smaller than the nanoparticle size for both GC and CS samples. The aggregation of several crystallites forms the nanoparticle. The comparison of average crystallite size and particle size of GS and CS samples verified the aggregation of crystallites in nanoparticles. The crystallite size and particle size of GS samples were much smaller than the CS samples. Considering the crystallite size and particle size in both CS and GS samples revealed that the particles in CS samples formed with aggregation of more numbers of crystallites compared to GS samples. Less agglomeration of crystallites in the presence of plant extract can be attributed to the capping role of the plant extract.

Figure 2 shows the FTIR spectra of produced iron oxides through green and chemical methods. The peaks between 530 and 670 cm^{-1} are related to the stretching vibration mode of Fe–O [29]. Different peaks in the range of 500 to 750 cm^{-1}, including peaks at 552.51, 564.07, 625.31, and 634.95 cm^{-1}, were observed in CS samples in the precursor concentrations 70 and 140 mM, showing various phases with Fe–O bonds, supporting the XRD results. Single sharp and broad peak was obtained at 552.51 cm^{-1} by increasing the concentration of precursor to 200 mM, implying the existence of a single phase with Fe–O bond. The XRD results revealed that the single phase is $\alpha - Fe_2O_3$.

A unique broad peak appeared at 632.06 cm^{-1} for all samples of GS, which shows the single phase of the iron compound. The sharper and broader peak observed in the FTIR results in a higher salt concentration than the other two. Similar broad peaks between the GS samples and myrtle extract at wave numbers 1632.64 and 3440.56 cm^{-1} verify the common functional groups between synthesized Fe_3O_4 nanoparticles and the myrtle extract. The formed peaks at wave numbers 1632.64 and 3440.56 cm^{-1} corresponded to the C = O or FeOO − and hydroxyl (-OH) functional groups, respectively

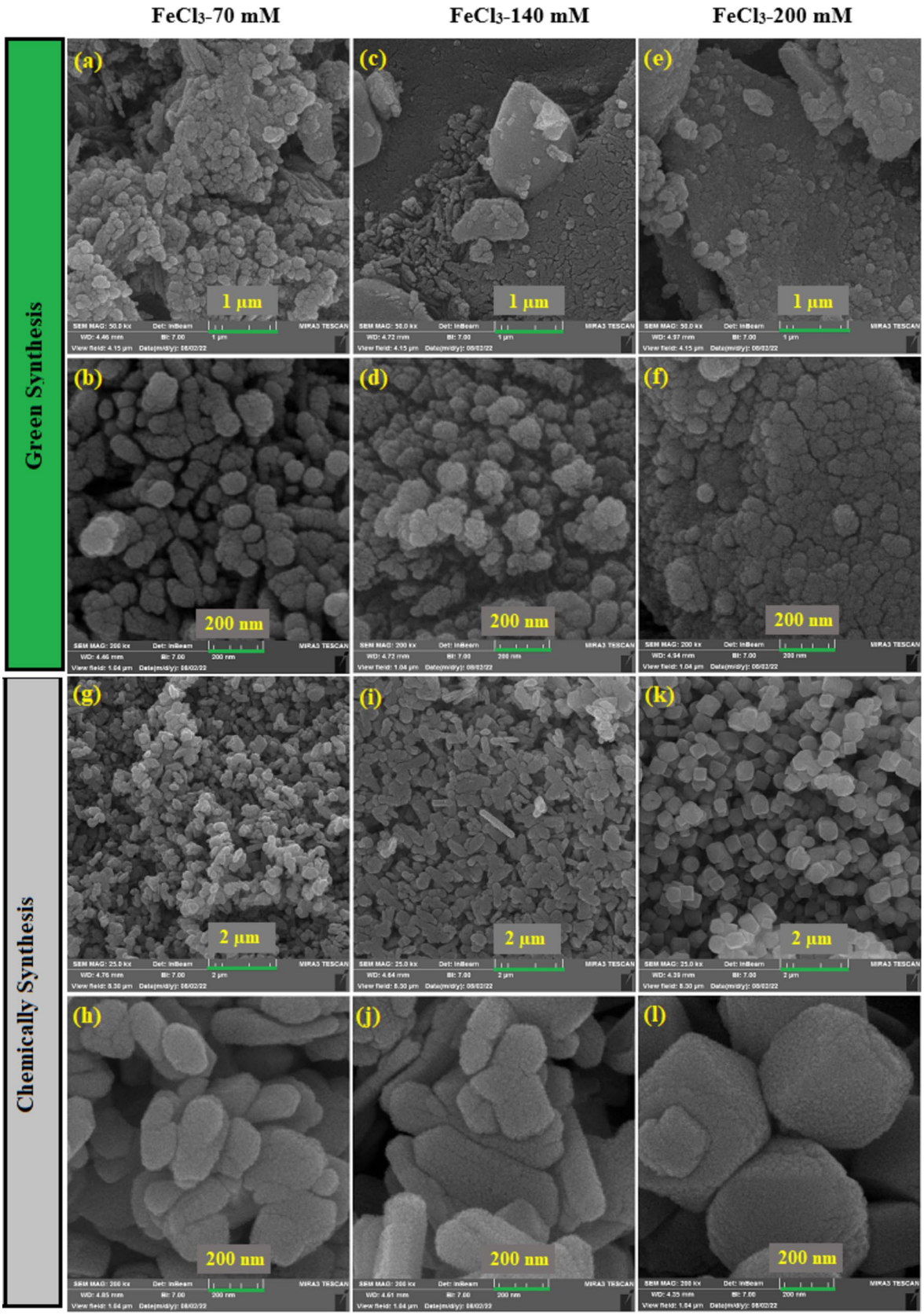

Fig. 3 SEM images of fabricated iron oxides. Green method (**a–f**) and chemical method (**g–l**)

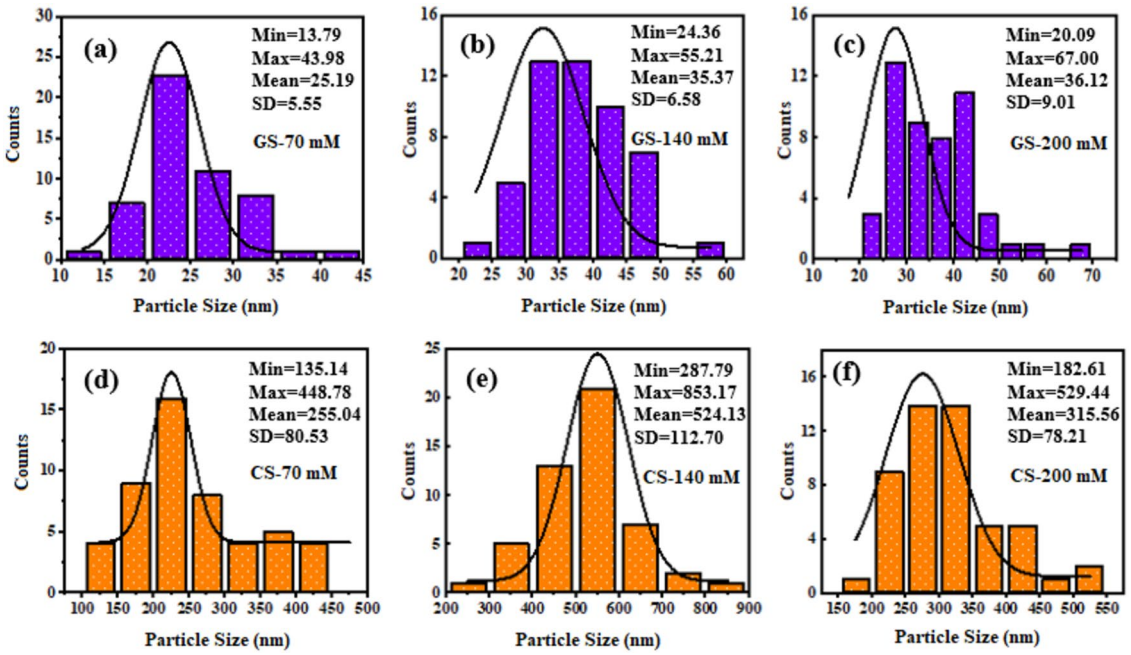

Fig. 4 Size distributions of (**a**–**c**) synthesized Fe_3O_4 nanoparticles and (**d**–**f**) the products of chemical method

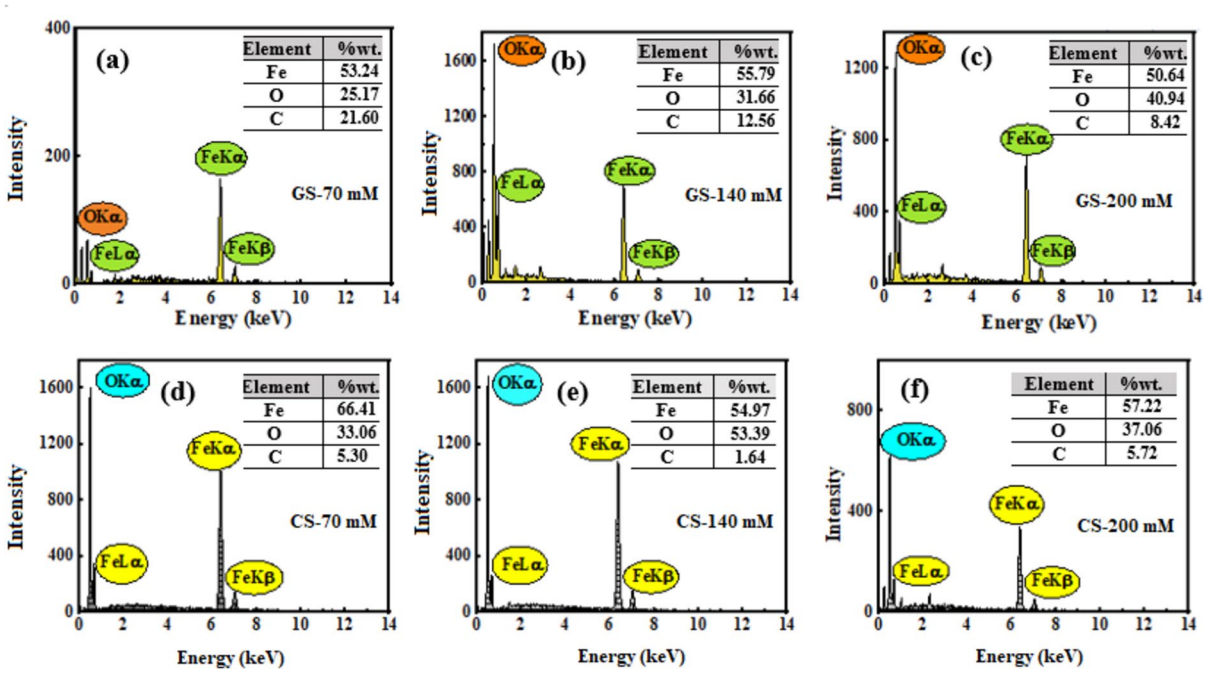

Fig. 5 EDS spectrum of synthesized iron oxides (**a**–**c**) with and (**d**–**f**) without plant intervention

[30, 31]. In contrast, these peaks did not appear in the FTIR spectrum of the CS samples.

3.2 Intervention of Plant Extract on Morphology and Size Distribution of Fabricated Iron Oxides

The FE-SEM images of fabricated iron oxides are presented in Fig. 3. As observed in Fig. 3a–f, the green synthesized

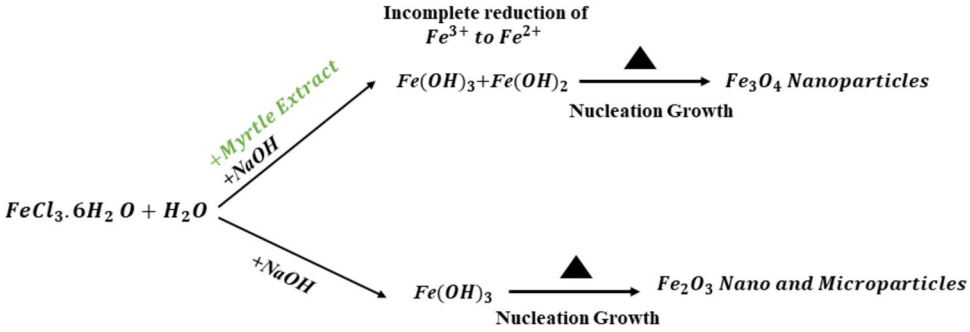

Fig. 6 Probable mechanism of produced Fe_3O_4 and Fe_2O_3 via green and chemical methods, respectively

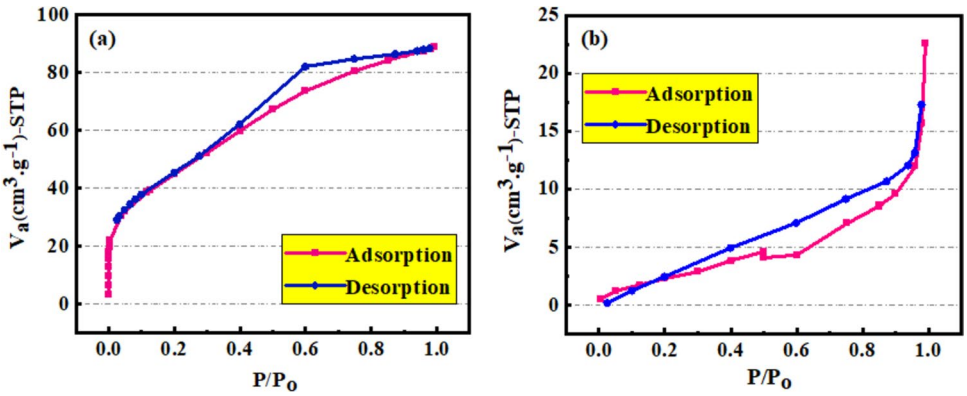

Fig. 7 Isotherms in N_2 adsorption–desorption of (**a**) Fe_3O_4 nanoparticles and (**b**) Fe_2O_3 microparticles

iron oxides formed the sphere-shaped aggregated Fe_3O_4 nanoparticles. This result reflects that the concentration of iron chloride does not affect the morphology of the formed particles. Therefore, the observation of similar morphology in green synthesized iron oxide confirms the importance of the extract as a capping and shape-controlling agent of the formed nanoparticles. Other researches also reported the spherical Fe_3O_4 nanoparticles in the presence of some plant extracts [32–34].

Conversely, the shape of particles changed with increasing salt concentration in chemically synthesized iron oxide particles. In a low concentration of iron chloride, a mixture of sphere-, rod-, sheet-, and rectangle-shaped particles has been observed (Fig. 3g–h). The mixture of cube- and rod-shaped particles was created in a medium salt concentration (Fig. 3i–j). Pure cube-shaped particles were obtained in a high concentration of salt (Fig. 3k–l). In this case, the pure cubic α-Fe_2O_3 was formed in a 200 mM in chemical synthesis. In contrast, in lower concentrations of salt solution, the mixture of different phases including FeOOH and Fe_2O_3 with different morphologies was produced.

The ImageJ software was used to estimate the particle size based on the SEM images. The size distribution of nanoparticles is presented in Fig. 4. In GS samples (Fig. 4a–c), the diameter of spheres was measured. However, the length of the rods was measured for rod-shaped particles. For this reason, the maximum size appeared in a chemical approach

Table 1 BET surface area, pore volume, and pore diameter of produced iron oxides with and without plant intervention

Sample	Green synthesis	Chemically synthesis
Type of iron oxide	Fe_3O_4	α-Fe_2O_3
BET surface area m^2/g	165.000	10.007
Pore volume cm^3/g	0.137	0.034
Mean pore diameter (nm)	3.332	13.672

in the iron chloride of 140 mM. In addition, for this concentration, the width of the rods was less than 100 nm. The mean size of particles in green synthesis is smaller than chemical method. Therefore, small spherical particles will be formed in the presence of biomolecules such as phenolic and flavonoid compounds [35, 36]. However, interpreting the trend change of the particle size in CS samples is difficult due to their different phase and compounds of iron oxides.

3.3 The Elemental Composition of Produced Iron Oxides

The EDS spectra and weight proportion of three elements (Fe, O, and C) were presented in Fig. 5. The result revealed the presence of carbon, iron, and oxygen elements in the GS samples. The highest content of Fe and O elements

Table 2 Comparative data analysis of BET of produced Fe_3O_4 nanoparticles with different precursors and methods

Precursor	Synthesis method	specific surface area—$m^2.g^{-1}$	Average pore size—nm	Particle size—nm	References
$FeCl_2{\cdot}4H_2O$ $FeCl_3{\cdot}6H_2O$ NaOH	Co-precipitation	100.52	24.40	10	[42]
$FeCl_3{\cdot}6H_2O$ CH_3COONa Ethylenediamine Ethylene Glycol	Hydrothermal	114.00	–	30	[43]
$FeSO_4{\cdot}7H_2O$ $FeCl_3{\cdot}6H_2O$ NaOH	Co-precipitation	25.20	14.4	–	[44]
$FeSO_4.7H_2O$ NaOH	Green synthesis	114.42	–	25	[45]
$FeCl_3{\cdot}6H_2O$ Sodium acetate	Green synthesis	10.88	0.07	–	[46]
$FeCl_2{\cdot}4H_2O$ $FeCl_3{\cdot}6H_2O$ HCl–KMnO4	Green synthesis	46.86	0.21	36.5	[47]
$FeCl_3$–FeSO4 NaOH	Green synthesis	150	–	5	[48]
$FeCl_3.6H_2O$ NaOH	Green synthesis	165	0.137		This research

confirms the formation of iron oxide nanoparticles [37]. In addition, the carbon content has been found to be around 21, 13, and 9% in the synthesized Fe_3O_4 nanoparticles with 70, 140, and 200 mM iron chloride, respectively. The existence of low-intensity signals of carbon in the EDS spectra of chemically Fe_2O_3 nanoparticles is due to the FE-SEM sample preparation. However, the presence of the higher intensity peaks of carbon in synthesized samples

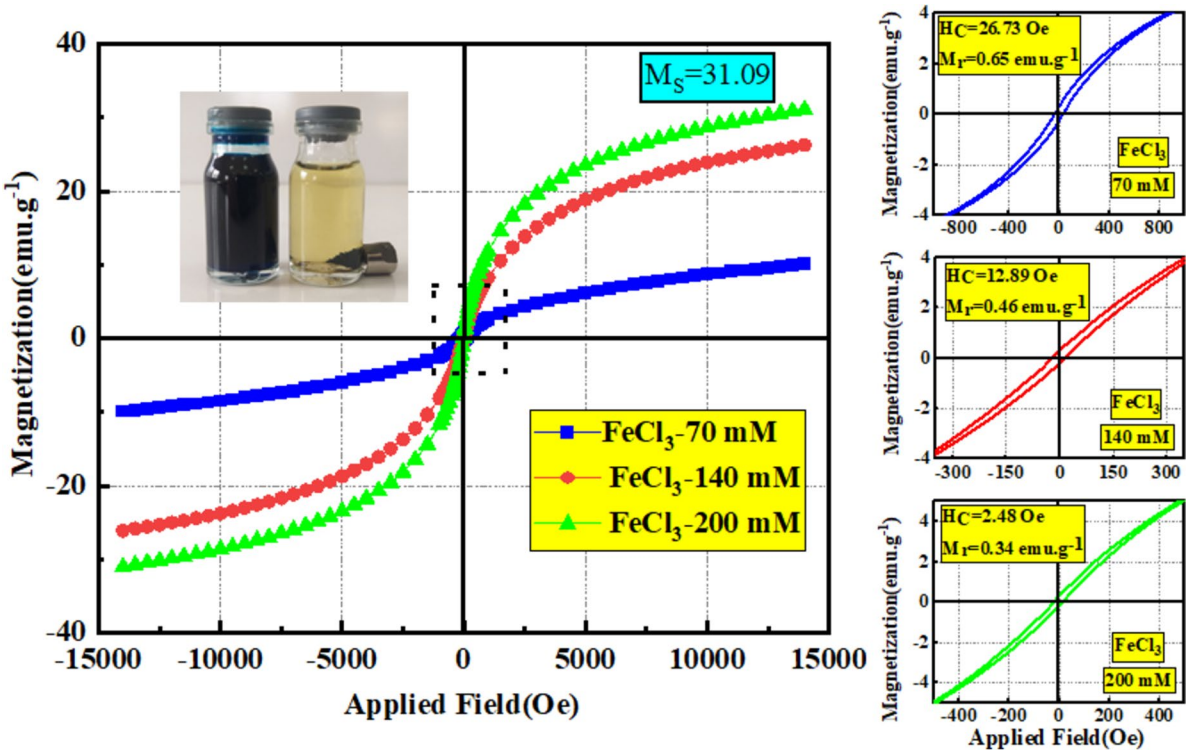

Fig. 8 VSM curves of green synthesized Fe_3O_4 nanoparticles

is attributed to the carbon of phenolic and flavonoid compounds of extract as a capping agent [38]. As mentioned, based on the production of two types of iron oxide in the chemical and green methods, the following possible mechanism has been proposed for Fe_3O_4 nanoparticles formation (Fig. 6). Iron chloride salt was the only precursor of iron oxide synthesized in this reaction. The iron ions in the iron chloride solution are in the form of Fe^{3+}, and on the other hand, it is clear that there are two forms of iron ions, including Fe^{3+} and Fe^{2+}, in the Fe_3O_4 compound. Therefore, the type of synthesized iron oxide confirms the simultaneous presence of both Fe^{3+} and Fe^{2+} ions in the reaction solution, leading to the formation of Fe_3O_4 nanoparticles due to the partial reduction of iron ions (Fe^{3+} to Fe^{2+}). Therefore, it can be concluded that the formation of black Fe_3O_4 is the result of the reduction of the initial ions in the presence of extract [39].

3.4 The Effect of Plant Extract in Formation of a Mesoporous Structure

Figure 7 presents the BET nitrogen adsorption/desorption isotherm curves of the as-prepared Fe_3O_4 and Fe_2O_3 nanoparticles. The isotherm curves closely match to a typical type IV isotherm graph with type H3 hysteresis loop, thereby confirming the mesoporous structure of the Fe_3O_4 nanoparticles [40, 41]. On the other hand, the isotherm of the synthesized Fe_3O_4 nanoparticles shows a step at relative pressure between 0.5 and 0.7, suggesting a narrow pore size distribution. As shown in Table 1, the Fe_3O_4 nanoparticles had a larger surface area than Fe_2O_3 particles. In addition, the mean pore diameter and pore volume of the synthesized Fe_3O_4 nanoparticles were lower and higher, respectively, than the Fe_2O_3 particles.

In brief, the role of myrtle extract in the synthesis is, first, changing the reaction path, leading to the formation of Fe_3O_4 nanoparticles rather than Fe_2O_3. Second, it affects the morphology of the nanoparticles by acting as a capping agent. Third, it causes a high increment of porosity and surface area of the product. A comparative analysis of the maximum BET surface area of various studies is reported in Table 2.

3.5 Effect of Iron Chloride Concentration on Magnetic Properties of Synthesized Fe_3O_4 Nanoparticles with a Green Approach

VSM analysis was applied to measure the magnetic properties of the mesoporous synthesized Fe_3O_4 nanoparticles. The saturation magnetization (M_s) was estimated by cycling the field between − 15 kOe and 15 kOe at 300 K. Figure 8 shows the hysteresis loop of synthesized Fe_3O_4 nanoparticles at three concentrations of salt. The highest saturation magnetization (31.09 emu.g^{-1}) is related to synthesized Fe_3O_4 nanoparticles at the high concentration of iron chloride. In green synthesis, at a constant volume ratio of myrtle extract to salt solution, the saturation magnetization (M_s) increased with the concentration of salt. As discussed before, the XRD analysis verified the phase purity of Fe_3O_4 nanoparticles. The result of the XRD pattern agrees with the VSM analysis because the pure and well-crystallized Fe_3O_4 nanoparticles were observed at the high concentration of salt with the high M_s value. Fe_3O_4 nanoparticles were easily separated from the solution using a magnet after adsorption process (Fig. 8). The paramagnetic was confirmed using VSM curves of green synthesized Fe_3O_4 nanoparticles, and it was evident by an extremely narrow hysteresis loop and slight remanence and coercivity. Moreover, the critical size for paramagnetic properties of Fe_3O_4 nanoparticles was estimated to be 20 nm [49], which is close to the size of the nanoparticles in this study. On the other hand, the critical size for the multidomain structure of spherical nanoparticles was theoretically calculated to be 128 nm which is larger than GS nanoparticles [50].

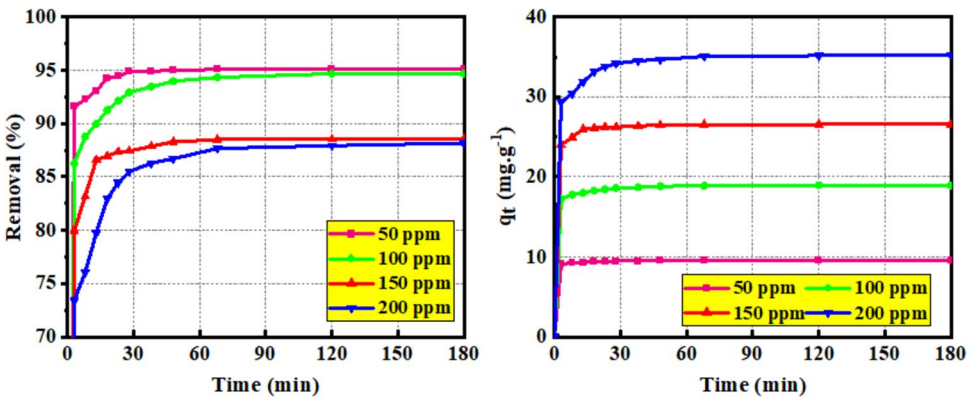

Fig. 9 MG dye removal and adsorption capacity using produced Fe_3O_4 nanoparticles

Table 3 Dye adsorption capacity of some adsorbents based on Fe_3O_4 nanoparticles

Nanoparticles	Synthesis method	Dye adsorption (mg.g^{-1})	References
GO/Fe_3O_4	Co-precipitation of Fe^{2+} and Fe^{3+} composited with graphene oxide in alkaline pH	30.30	[56]
Fe_3O_4@chitosan@ZIF-8	Mixing of acetic acid, chitosan, Fe_3O_4 nanoparticles, and ZIF-8	3.28	[57]
Fe_3O_4@SiO_2–NH_2	Co-precipitation of Fe^{2+} and Fe^{3+}	173.00	[58]
Alginate-coated Fe_3O_4	Co-precipitation of Fe^{2+} and Fe^{3+} coated with alginate	47.84	[59]
Fe_3O_4/polystyrene–alginate	Mixing Fe_3O_4/Polystyrene composite with alginate solution and cross-linking using $CaCl_2$	34.12	[60]
Fe_3O_4	Green synthesis	35.44	This research

3.6 MG Adsorption using Fe_3O_4 Nanoparticles

The dye removal results are presented in Fig. 9. The pH of the dye solution is one of the most critical factors that confine the adsorption property because of its effect not only on the surface charge of the adsorbent but also on the ionization degree of the adsorbent. Since the maximum adsorption was observed at pH 7.0, this pH was selected for all experiments [51]. The MG adsorption capacity raised with increasing the initial dye concentration and exhibited a time-dependent process for all dye concentrations. In the initial 30 min, the percent removal of MG sharply increased close to the maximum adsorption (about 95%) for concentrations of 50 and 100 ppm. For two other concentrations (150 and 200 ppm), the percentage removal was about 85% in the same contact time (30 min). The percent of dye removal decreased (95–85%) with increasing the initial dye concentration due to increasing the MG onto the nanoparticles in the first times, which leads to decreasing the active sites onto the nanoparticles to uptake the dye molecules. A similar result was reported by Abewaa et al. [52].

The adsorption equilibrium was obtained in about 60 min for two low concentrations. The dye concentration gradually decreased during the same time for initial concentrations of 150 and 200 ppm. Moreover, the equilibrium time of the dye concentrations of 150 and 200 ppm was longer (120 min) than the two other concentrations. The maximum adsorbed dye was obtained 35.44 mg.g^{-1} in a 200 ppm MG concentration after 120 min.

Improving porosity and functionalizing the surface of nanoparticles are two important techniques for maximizing the dye adsorption capacity. Bonyadi et al. improved the adsorption capacity of iron oxide nanoparticle-loaded sawdust carbon (Fe_3O_4/SC) to 41.66 mg.g^{-1} [53]. The maximum adsorption capacity of the MG was reported 47.84 mg.g^{-1} using Fe_3O_4 nanoparticles, in which surface of nanoparticles was coated with sodium alginate (Alg–Fe_3O_4) by Mohammadi et al. [54]. In our study, the authors used a single iron salt with the myrtle extract to produce mesoporous Fe_3O_4 adsorbents with high adsorption and magnetic properties. The Fe_3O_4 nanoparticles tend to adsorb cationic ions due to their negatively charged surface [55]. On the other hand, the presence of carbon and -OH functional groups in biomolecules of extract and the contribution of these compounds led to increasing the adsorption capacity.

The MG adsorption with Fe_3O_4-based adsorbent has been reported by other researchers. However, most of the adsorbents are the composites of magnetic iron oxide and other compounds with various dye adsorption capacities. On the other hand, they mostly used chemical methods for the

Table 4 Parameters of the kinetic models of MG adsorption onto green synthesized Fe_3O_4 nanoparticles

		Initial dye concentration			
	Factor	50	100	150	200
Pseudo-first-order	$q^*_{max(}$Experimental$_)$—mg.g^{-1}	9.51	18.94	26.54	35.26
	$q_{max\ (}$Calculated$_)$—mg.g^{-1}	1.17	2.45	2.58	6.18
	K_1—min^{-1}	0.11	0.149	0.06	0.04
	R-Square	0.80	0.88	0.82	0.81
Pseudo-second-order	$q_{max\ (}$Calculated$_)$—mg.g^{-1}	9.52	18.99	26.62	35.44
	K_2—g·mg^{-1}·min^{-1}	0.75	0.10	0.12	0.03
	R-Square	1.00	0.99	0.99	0.99
IPD	*B*—mg.g^{-1}	6.60	12.56	17.84	21.81
	K_{ID}—g·mg^{-1}·$min^{-0.5}$	0.36	0.76	1.05	1.55
	R-Square	0.25	0.29	0.28	0.36

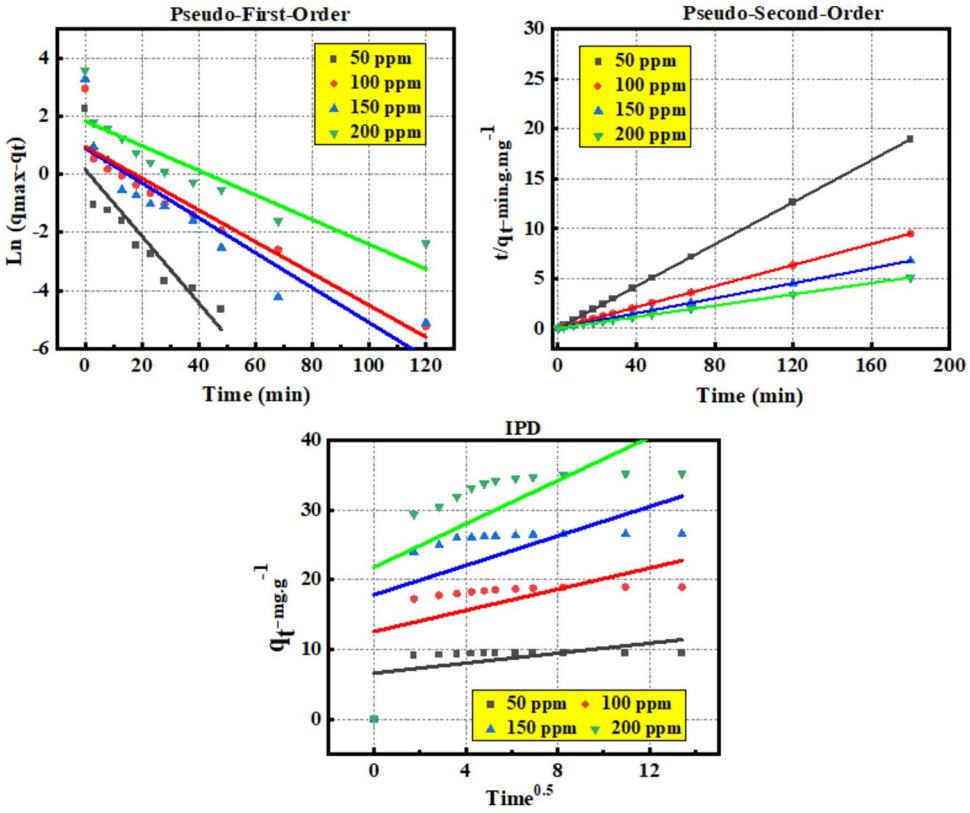

Fig. 10 Plots of the kinetic models of MG adsorption onto synthesized Fe_3O_4 nanoparticles

synthesis of Fe_3O_4 composites. Therefore, the precise comparison is not applicable. Nevertheless, the results of some studies are listed in Table 3. The dye adsorption capacity of GS nanoparticles in this study is comparable with most researches. Considering the advantages such as one-facile-step fabrication and an environmentally friendly method, and using the green synthesized Fe_3O_4 nanoparticles rather than complicated composites, one can conclude the superiority of the green synthesized nanoparticles in MG adsorption.

To understand the kinetic model of the MG adsorption, pseudo-first-order, pseudo-second-order, and intra-particle diffusion (IPD) models were studied [61, 62]. The pseudo-first-order kinetic model is described in Eq. 4:

$$\mathrm{Ln}\left(q_{\max} - q_t\right) = \mathrm{Ln}q_{\max} - K_1 \mathrm{t} \tag{4}$$

where K_1 (min^{-1}) is rate constant of adsorption in this model, and $q_{\max}$ and q_t are the adsorption capacity of nanoparticles to remove the MG dye per gram of adsorbent (mg.g^{-1}) at equilibrium and every moment, respectively.

The adsorption result was further evaluated using a pseudo-second-order kinetic model. The linearized form of the equation can be signified as follows:

$$\frac{t}{q_\mathrm{t}} = \frac{1}{K_2 q_{\max}^2} + \frac{t}{q_{\max}} \tag{5}$$

where K_2 (g.min^{-1}.mg^{-1}) is the rate constant of MG adsorption in the pseudo-second-order equation, $q_{\max}$ and q_t is the same as Eq. 4. In addition, the intra-particle diffusion (IPD) was studied as the last kinetic model to evaluate the adsorption data which is described by Eq. 6:

$$q_t = K_{ID}\sqrt{t} + B \tag{6}$$

where K_{ID} (mg.$\mathrm{min}^{-0.5}$.g^{-1}) is the rate constant of the IPD kinetic model and B is the same unit as q_t (mg.g^{-1}) as an intercept of Eq. 6.

According Table 4, the calculated $q_{\max}$ from pseudo-second-order model was 9.52, 18.99, 26.62, and 35.44 mg.g^{-1} for 50, 100, 150, and 200 ppm dye concentrations, respectively, which is acceptably close to experimental $q_{\max}$. Therefore, MG adsorption data fitted well with the pseudo-second-order model at all MG concentrations (Fig. 10).

4 Conclusions

The inclusion of plant extract facilitated the synthesis of Fe_3O_4 nanoparticles. The SEM images explored the green approach which led to the formation of spherical Fe_3O_4, exhibiting homogeneity in particle distribution. The average particle size was approximately 36 nm. In contrast, the absence of plant extract resulted in the formation of

cube-shaped α-Fe_2O_3 particles. The paramagnetic nature of prepared Fe_3O_4 nanoparticles was confirmed by VSM analysis, with an increase in paramagnetic properties (31.09 emu.g^{-1}) observed upon augmenting the iron salt concentration in the reaction solution. Furthermore, the Fe_3O_4 nanoparticles synthesized exhibited a specific surface area of 165 $m^2.g^{-1}$ and an average pore size of 3.32 nm, indicating the formation of mesoporous structures. The MG adsorption studies demonstrated a maximum adsorption capacity of 35.44 mg.g^{-1}. Thus, the presence of plant extract played a pivotal role in controlling the shape, size, porosity, pore size, and magnetic properties of produced iron oxides. Consequently, the synthesized Fe_3O_4 nanoparticles exhibited promising potential as highly efficient adsorbents with notable dye removal efficiency and satisfactory paramagnetic properties in the wastewater treatment.

Declarations

Conflicts of interest The authors declare no conflict of interest.

References

1. Kumar K Y, Muralidhara H B, Nayaka Y A, Balasubramanyam J, and Hanumanthappa H, *Powder Technol* **246** (2013) 125. https://doi.org/10.1016/j.powtec.2013.05.017
2. Liu X, Tian J, Li Y, Sun N, Mi S, Xie Y, and Chen Z, *J Hazard Mater* **373** (2019) 397. https://doi.org/10.1016/j.jhazmat.2019.03.103
3. Srivastava S, Sinha R, and Roy D, *Aquat Toxicol* **66** (2004) 319. https://doi.org/10.1016/j.aquatox.2003.09.008
4. Song J, Han G, Wang Y, Jiang X, Zhao D, Li M, Yang Z, Ma Q, Parales R E, Ruan Z, and Mu Y, *Sci Rep* **10** (2020) 4502. https://doi.org/10.1038/s41598-020-61442-z
5. Hameed B H, and El-Khaiary M I, *J Hazard Mater* **159** (2008) 574. https://doi.org/10.1016/j.jhazmat.2008.02.054
6. Gharavi-Nakhjavani M S, Niazi A, Hosseini H, Aminzare M, Dizaji R, Tajdar-Oranj B, and Mirza Alizadeh A, *Environ Sci Pollut Res* **30** (2023) 48911. https://doi.org/10.1007/s11356-023-26285-x
7. Araki J, *Cellulose* **28** (2021) 7707. https://doi.org/10.1007/s10570-021-04035-x
8. Yin G, Sun Z, Gao Y, and Xu S, *Microchem J* **166** (2021) 106190. https://doi.org/10.1016/j.microc.2021.106190
9. Sahoo S K, Panigrahi G K, Dhal J P, Sahoo J K, Biswal S K, Sahoo A, Subhalaxmi S, Sahoo D M, Mohapatra L, Mahakul M M, and Sahoo A, *Inorg Chem Commun* (2023). https://doi.org/10.1016/j.inoche.2023.110969
10. Salleh M A, Mahmoud D K, Karim W A, and Idris A, *Desalination* **280** (2011) 1. https://doi.org/10.1016/j.desal.2011.07.019
11. Moosavi S, Lai C W, Gan S, Zamiri G, Akbarzadeh Pivehzhani O, and Johan M R, *ACS Omega* **5** (2020) 20684.
12. Das S K, and Chatterjee M K, *Bull Mater Sci* **16** (1993) 205. https://doi.org/10.1007/BF02745146
13. Uheida A, Salazar-Alvarez G, Björkman E, Yu Z, and Muhammed M, *J Colloid Interface Sci* **298** (2006) 501. https://doi.org/10.1016/j.jcis.2005.12.057
14. Babay S, Mhiri T, and Toumi M, *J Mol Struct* **1085** (2015) 286. https://doi.org/10.1016/j.molstruc.2014.12.067
15. Bassim S, Mageed A K, AbdulRazak A A, and Al-Sheikh F, *Bull Chem React Eng Catal* **18** (2023) 1. https://doi.org/10.9767/bcrec.16417
16. Mehdizadeh A, Najafi Moghadam P, Ehsanimehr S, and Fareghi A R, *Mater Chem Horiz* **1** (2022) 23.
17. Araghi S H, Entezari M H, and Chamsaz M, *Microporous Mesoporous Mater* **218** (2015) 101. https://doi.org/10.1016/j.micromeso.2015.07.008
18. Horák D, Trchová M, Beneš M J, Veverka M, and Pollert E, *Polymer* **51** (2010) 3116. https://doi.org/10.1016/j.polymer.2010.04.055
19. Karunakaran S, Ramanujam S, and Gurunathan B, *IET Nanobiotechnol* **12** (2018) 1003. https://doi.org/10.1049/iet-nbt.2018.5048
20. Yaghoobi M, Asjadi F, and Sanikhani M, *J Taiwan Inst Chem Eng* **144** (2023) 104774. https://doi.org/10.1016/j.jtice.2023.104774
21. Zhang Y, Luo D, Wu P, Liu C, He J, and Jiang W, *J Iran Chem Soc* **20** (2023) 2665. https://doi.org/10.1007/s13738-023-02864-0
22. Barakat M A, Kumar R, Lima E C, and Seliem M K, *J Taiwan Inst Chem Eng* **119** (2021) 146. https://doi.org/10.1016/j.jtice.2021.01.025
23. Zhuang L, Zhang W, Zhao Y, Shen H, Lin H, and Liang J, *Sci Rep* **5** (2015) 9320. https://doi.org/10.1038/srep09320
24. Tang X, Li Z, Liu K, Luo X, He D, Ao M, and Peng Q, *Powder Technol* **376** (2020) 42. https://doi.org/10.1016/j.powtec.2020.08.018
25. Zhu Y, Peng C, Gao Z F, Yang H, Liu W M, and Wu Z J, *J Environ Chem Eng* **6** (2018) 3358. https://doi.org/10.1016/j.jece.2018.05.012
26. Tadic M, Trpkov D, Kopanja L, Vojnovic S, and Panjan M, *J Alloys Compd* **792** (2019) 599. https://doi.org/10.1016/j.jallcom.2019.03.414
27. Bouziani A, Park J, and Ozturk A, *J Photochem Photobiol A Chem* **400** (2020) 112718. https://doi.org/10.1016/j.jphotochem.2020.112718
28. Jo W K, Park G T, and Tayade R J, *J Chem Technol Biotechnol* **90** (2015) 2280. https://doi.org/10.1002/jctb.4547
29. Bonesio M D, Nogueira F G, Mancini D T, Ribeiro L S, and Ramalho T C, *J Iran Chem Soc* **20** (2023) 415. https://doi.org/10.1007/s13738-022-02676-8
30. He G, Liu W, Sun X, Chen Q, Wang X, and Chen H, *Mater Res Bull* **48** (2013) 1885. https://doi.org/10.1016/j.materresbull.2013.01.038
31. Dehghan Z, Ranjbar M, Govahi M, and Khakdan F, *J Drug Deliv Sci Technol* **67** (2022) 102941. https://doi.org/10.1016/j.jddst.2021.102941
32. Hussain I, Singh N B, Singh A, Singh H, and Singh S C, *Biotechnol Lett* **38** (2016) 545. https://doi.org/10.1007/s10529-015-2026-7
33. Kumar B, Smita K, Cumbal L, and Debut A, *J Saudi Chem Soc* **18** (2014) 364. https://doi.org/10.1016/j.jscs.2014.01.003
34. Yew Y P, Shameli K, Miyake M, Kuwano N, Bt Ahmad Khairudin N B, Bt Mohamad S E, and Lee K X, *Nanoscale Res Lett* **11** (2016) 1. https://doi.org/10.1186/s11671-016-1498-2
35. Ahmad T, Bustam M A, Irfan M, Moniruzzaman M, Asghar H M, and Bhattacharjee S, *J Mol Struct* **1159** (2018) 167. https://doi.org/10.1016/j.molstruc.2017.11.095
36. Sundrarajan M, Bama K, Bhavani M, Jegatheeswaran S, Ambika S, Sangili A, Nithya P, and Sumathi R, *J Photochem Photobiol*

B Biol **171** (2017) 117. https://doi.org/10.1016/j.jphotobiol.2017.05.003
37. Rahman S S, Qureshi M T, Sultana K, Rehman W, Khan M Y, Asif M H, Farooq M, and Sultana N, *Results Phys* **7** (2017) 4451. https://doi.org/10.1016/j.rinp.2017.11.001
38. Ullah A, and Lim S I, *Biotechnol Bioeng* **119** (2022) 2273. https://doi.org/10.1002/bit.28148
39. Lomozová Z, Hrubša M, Conte P F, Papastefanaki E, Moravcova M, Catapano M C, Silvestri I P, Karlíčková J, Kučera R, Macáková K, and Mladěnka P, *Food Chem* **394** (2022) 133461. https://doi.org/10.1016/j.foodchem.2022.133461
40. Al-Salihi S, Bayati M, Jasim A M, Fidalgo M M, and Xing Y, *Environ Adv* **9** (2022) 100283. https://doi.org/10.1016/j.envadv.2022.100283
41. Wahab M A, Darain F, Karim M A, and Beltramini J N, *Int J Electrochem Sci* **10** (2015) 7732.
42. Iconaru S L, Guégan R, Popa C L, Motelica-Heino M, Ciobanu C S, and Predoi D, *Appl Clay Sci* **134** (2016) 128. https://doi.org/10.1016/j.clay.2016.08.019
43. Sani S, Adnan R, Oh W D, and Iqbal A, *Nanomater* **11** (2021) 2742. https://doi.org/10.3390/nano11102742
44. Mozaffari M, Khodabakhshi A, and Azizi A, *J Chem* (2023). https://doi.org/10.1155/2023/7011995
45. Pai S, Kini S M, Narasimhan M K, Pugazhendhi A, and Selvaraj R, *Surf Interfaces* **23** (2021) 100947. https://doi.org/10.1016/j.surfin.2021.100947
46. Venkateswarlu S, Kumar B N, Prathima B, SubbaRao Y, and Jyothi N V, *Arab J Chem* **12** (2019) 588. https://doi.org/10.1016/j.arabjc.2014.09.006
47. Taqui M, Das S, Kamilya T, Mondal S, and Chaudhuri S, *J Environ Eng Landsc Manag* **30** (2022) 308. https://doi.org/10.3846/jeelm.2022.16747
48. Alajmi M F, Ahmed J, Hussain A, Ahamad T, Alhokbany N, Amir S, Ahmad T, and Alshehri S M, *Appl Nanosci* **8** (2018) 1427. https://doi.org/10.1007/s13204-018-0795-8
49. Li Q, Kartikowati C W, Horie S, Ogi T, Iwaki T, and Okuyama K, Correlation between particle size/domain structure and magnetic properties of highly crystalline Fe_3O_4 nanoparticles. *Sci Rep* **7** (2017) 9894. https://doi.org/10.1038/s41598-017-09897-5
50. Leslie-Pelecky D L, and Rieke R D, Magnetic properties of nanostructured materials. *Chem Mater* **8** (1996) 1770. https://doi.org/10.1021/cm960077f
51. Li W, Xu M, Cao Q, Luo J, Yang S, and Zhao G, *RSC Adv* **11** (2021) 19387. https://doi.org/10.1039/D1RA02209A
52. Abewaa M, Mengistu A, Takele T, Fito J, and Nkambule T, *Sci Rep* **13** (2023) 14701. https://doi.org/10.1038/s41598-023-41957-x
53. Bonyadi Z, Khatibi F S, and Alipour F, *Appl Water Sci* **12** (2022) 221. https://doi.org/10.1007/s13201-022-01745-w
54. Mohammadi A, Daemi H, and Barikani M, *Int J Biol Macromol* **69** (2014) 447. https://doi.org/10.1016/j.ijbiomac.2014.05.042
55. Chatterjee S, Guha N, Krishnan S, Singh A K, Mathur P, and Rai D K, *Sci Rep* **10** (2020) 111. https://doi.org/10.1038/s41598-019-57017-2
56. Li W, Xu M, Cao Q, Luo J, Yang S, and Zhao G, Magnetic GO/Fe_3O_4 for rapid malachite green (MG) removal from aqueous solutions: a reversible adsorption. *RSC Adv* **11** (2021) 19387. https://doi.org/10.1039/D1RA02209A
57. Zadvarzi S B, Khavarpour M, Vahdat S M, Baghbanian S M, and Rad A S, *Int J Biol Macromol* **168** (2021) 428. https://doi.org/10.1016/j.ijbiomac.2020.12.067
58. Sun L, Hu S, Sun H, Guo H, Zhu H, Liu M, and Sun H, *RSC Adv* **5** (2015) 11837.
59. Mohammadi A, Daemi H, and Barikani M, *Int J Biol Macromol* **69** (2014) 447. https://doi.org/10.1016/j.ijbiomac.2014.05.042
60. Mohammadi R, Massoumi B, Mashayekhi R, and Hosseinian A, *Iran J Chem Chem Eng* **41** (2022) 3632.
61. Zein R, Tomi Z B, Fauzia S, and Zilfa Z, *J Iran Chem Soc* **17** (2020) 2599. https://doi.org/10.1007/s13738-020-01955-6
62. Exley J M, Hunter T N, Pugh T, and Tillotson M R, *Powder Technol* **421** (2023) 118387. https://doi.org/10.1016/j.powtec.2023.118387